2D Vermiculite Nanolaminated Membranes for Efficient Organic Solvent Nanofiltration

Wensen Wang, Xishun Hao, Youguo Yan, Rong Sun, Eddy Petit, Mathilde Moderne, Ji Li, Jiefeng Liu, Huali Wu, Kun Qi, et al.

ADVANCED FUNCTIONAL MATERIALS
www.afm-journal.de

2D Vermiculite Nanolaminated Membranes for Efficient Organic Solvent Nanofiltration

*Wensen Wang, Xishun Hao, Youguo Yan, Rong Sun, Eddy Petit, Mathilde Moderne, Ji Li, Jiefeng Liu, Huali Wu, Kun Qi, Camilo Zamora-Ledezma, Christian Narváez-Muñoz, Camille Bakkali Hassani, Luc Lajaunie, Philippe Miele, Chrystelle Salameh, Zhiyuan Zeng, and Damien Voiry**

Membrane separation technology has found widespread application in molecular sieving and water reclamation. Its use in organic solvent nanofiltration (OSN) has been limited by the modest permeation rates and stability of existing membranes. In this study, 2D clay nanolaminated membranes are engineered, derived from the stacking of exfoliated vermiculite nanosheets, as a potential solution for OSN. The as-synthesized clay membrane displayed limited stability in both water and solvents due to rapid hydration or solvation of the nanosheets. To enhance the membrane's stability and sieving capabilities, cations of various valences (K^+, Na^+, Mg^{2+}, Ca^{2+}, Fe^{3+}) are intercalated into the interlayer of the clay nanosheets. The resulting cation-treated clay membranes display considerable enhancement in structural stability in both aqueous and organic media. Subsequently, the solvent transport behavior and separation performance of these clay membranes are evaluated and described by molecular dynamic simulation and experiments. It is identified that Fe-intercalated nanolaminates demonstrate controllable stacking order, resulting in enhanced sieving performance with a rejection rate of over 95% for Methyl Orange and a methanol permeation rate of ≈165 L m^{-2} h^{-1} bar^{-1} [LMHB]. The findings of this work pave the way for the practical applications of 2D nanolaminated clay membranes in OSN.

1. Introduction

Membrane separation technology has emerged as an environmentally friendly, performance-effective, energy-efficient, and easy-to-operate method, finding widespread use in water treatment applications such as sewage purification and seawater desalination.[1] Rational design of advanced materials, such as thin-film composite membranes, has facilitated their extensive use in the industry for aqueous separation.[2] Despite these advances, the application of membrane technology for organic solvent separation remains limited, primarily due to the weak chemical stability of most polymer membranes in organic solvents. Furthermore, low permeation rates and aging issues also hinder the widespread adoption of this technology.[3] Simultaneously, the rapidly expanding pharmaceutical and petrochemical industries are driving a strong demand for organic solvent treatment.[4] Consequently, there is an urgent need to

W. Wang, E. Petit, M. Moderne, J. Li, J. Liu, H. Wu, K. Qi, P. Miele, C. Salameh, D. Voiry
Institut Européen des Membranes
IEM
UMR 5635
Univ Montpellier
ENSCM
CNRS
Montpellier 34000, France
E-mail: damien.voiry@umontpellier.fr

The ORCID identification number(s) for the author(s) of this article can be found under https://doi.org/10.1002/adfm.202410635

DOI: 10.1002/adfm.202410635

X. Hao, Y. Yan
School of Materials Science and Engineering
China University of Petroleum
Qingdao 266580, P. R. China

R. Sun, L. Lajaunie
Departamento de Ciencia de los Materiales e Ingeniería Metalúrgica y Química Inorgánica
Instituto Universitario de Investigación de Microscopía Electrónica y Materiales (IMEYMAT)
Facultad de Ciencias
Universidad de Cádiz
Campus Río San Pedro S/N, Puerto Real, Cádiz 11510, Spain

C. Zamora-Ledezma
Higher Polytechnic School
UAX - Universidad Alfonso X el Sabio
Avda. Universidad 1, Villanueva de la Cañada 28691, Madrid, Spain

develop novel membranes that can address this technological gap and enhance the performance of membrane separation processes in organic solvents.

2D materials, characterized by atomic thickness in one direction and vast lateral dimensions in the other two, have garnered significant interest due to their exceptional properties and potential applications in various fields such as catalysis,[5] electronic conduction,[6] energy storage and conversion,[7] and, most importantly, membrane separation.[8] Nanolaminated membranes prepared by stacking 2D nanosheets form slit-type nanochannels between adjacent nanosheets, which regulate the transport of molecules and the nanofluidic behavior under sub-nanometer confinement.[9] With the rapid development of 2D materials, a library of 2D nanosheets has become available as building blocks for the construction of the nanolaminates.[10] MXene and transition metal dichalcogenides (TMDs) laminar membranes have demonstrated unparalleled flux for organic solvents and moderate rejection for larger dye molecules, highlighting the potential of 2D laminar membranes for organic solvent nanofiltration (OSN).[11] However, the fabrication of these 2D nanosheets remains complex, expensive, and reliant on the use of hazardous reagents, posing limitations on membrane applications and raising sustainability concerns.[12] Therefore, there is an urgent need to explore alternative 2D nanosheets that are cost-effective, easy to produce, and suitable for OSN applications.

Vermiculite clay, a natural mineral with a layered structure, can be easily exfoliated into 2D nanosheets using a simple ion exchange method.[13] Due to their exceptional chemical and mechanical stability, 2D clay nanosheets have garnered significant attention for constructing 2D laminar membranes.[14] Tian et al. demonstrated the suitability of 2D laminated clay membranes for OSN, opening a path toward low-cost 2D membrane construction for highly efficient separation applications. The high affinity of clay nanosheets for polar molecules however typically leads to uncontrollable interlayers spacing due to swelling as observed for GO and MXenes. It results in degradation of sieving performance. Employing a non-covalent modification strategy to introduce cations for enhancing membrane stability, without incurring additional defects, has demonstrated notable efficacy in graphene oxide (GO) and MXene membranes for water purification.[15] This approach capitalizes on the electrostatic interactions between intercalants and nanosheets to enhance the structural integrity of the laminates. Considering the negatively charged nature of clay nanosheets, such a method offers a potential solution for improving the stability of clay membranes against swelling and delamination.

In this work, we report the preparation of environmentally friendly nanolaminated membranes for organic solvent filtration. We exfoliated bulk natural clay vermiculite into single layers and reassembled them into 2D nanolaminated membranes. The organic solvent transport behavior and separation performance was investigated for the sieving of organic dye molecules. We found poor rejection efficiency from pristine vermiculite membranes using organic dye molecules due to increased interlayer spacing, suggesting that these membranes may not be suitable for organic solvent purification. To enhance the interlayers space stability and confer effective molecular sieving ability to the nanolaminates, different valence cations (K^+, Na^+, Mg^{2+}, Ca^{2+} and Fe^{3+}) were employed to intercalate into the interlayer of clay nanosheets. We identified that cation-treated vermiculite membranes exhibited limited swelling and improved membrane structural stability in both aqueous and organic phases. In particular, Fe-intercalated vermiculite nanolaminates displayed the strongest resistance against swelling, resulting in a superior sieving performance with a rejection rate of over 95% for Methyl Orange (MO, 327.33 Da) and a methanol permeation rate of ≈165 LMHB. Furthermore, we demonstrated over 100 h of constant operation under tangential cross-flow filtration conditions with a membrane size of 10 cm^2, paving the way for practical applications of nanolaminated organic solvent nanofiltration membranes.

2. Results and Discussions

2.1. Characterization of Nanolaminated Clay Membranes

Single-layer vermiculite nanosheets were first obtained by exfoliation of bulk vermiculite using Na^+ and Li^+ exchange methods, then collected by centrifugation. The single-layer nature of vermiculite nanosheets was demonstrated by atomic force microscopy (AFM) with a thickness of less than 2 nm, attributable to the hydrophilicity of the nanosheets (**Figure 1a**, height profile). The obtained nanosheets exhibit a micrometer-sized lateral surface (Figure 1a; Figure S1, Supporting Information). High-resolution transmission electron microscopy (HRTEM) and selected area diffraction patterns (SADP) (Figure 1b; Figure S1b, Supporting Information) were used to characterize the nanosheets, revealing an excellent crystallinity and structural data in good agreement with the vermiculite crystallographic cell (Figure S1c, Supporting Information).[16] The vermiculite nanosheets were stacked into nanolaminated membranes (called hereafter pristine clay membranes) using a pressure-assisted filtration strategy on porous substrates. The ordered laminar stacking of clay membranes was confirmed by a clear interstitial structure observed in scanning electron microscopy (SEM) cross-sectional views (Figure 1c). Cation-treated vermiculite nanolaminated membranes (called hereafter X-clay membranes, with X a metal cation) were prepared by adding the corresponding electrolyte solution to the pristine membrane and allowing cations to diffuse

C. Narváez-Muñoz
Centre Internacional de Mètodes Numérics en Enginyeria (CIMNE)
C/Gran Capitán s/n
Campus Nord UPC – Universitat Politècnica de Catalunya
Barcelona 08034, Spain

C. B. Hassani
ICGM
Université Montpellier
CNRS
ENSCM
Montpellier 34000, France

Z. Zeng
Department of Materials Science and Engineering
and State Key Laboratory of Marine Pollution
City University of Hong Kong
Hong Kong 999077, P. R. China

Z. Zeng
Shenzhen Research Institute
City University of Hong Kong
Shenzhen 518057, P. R. China

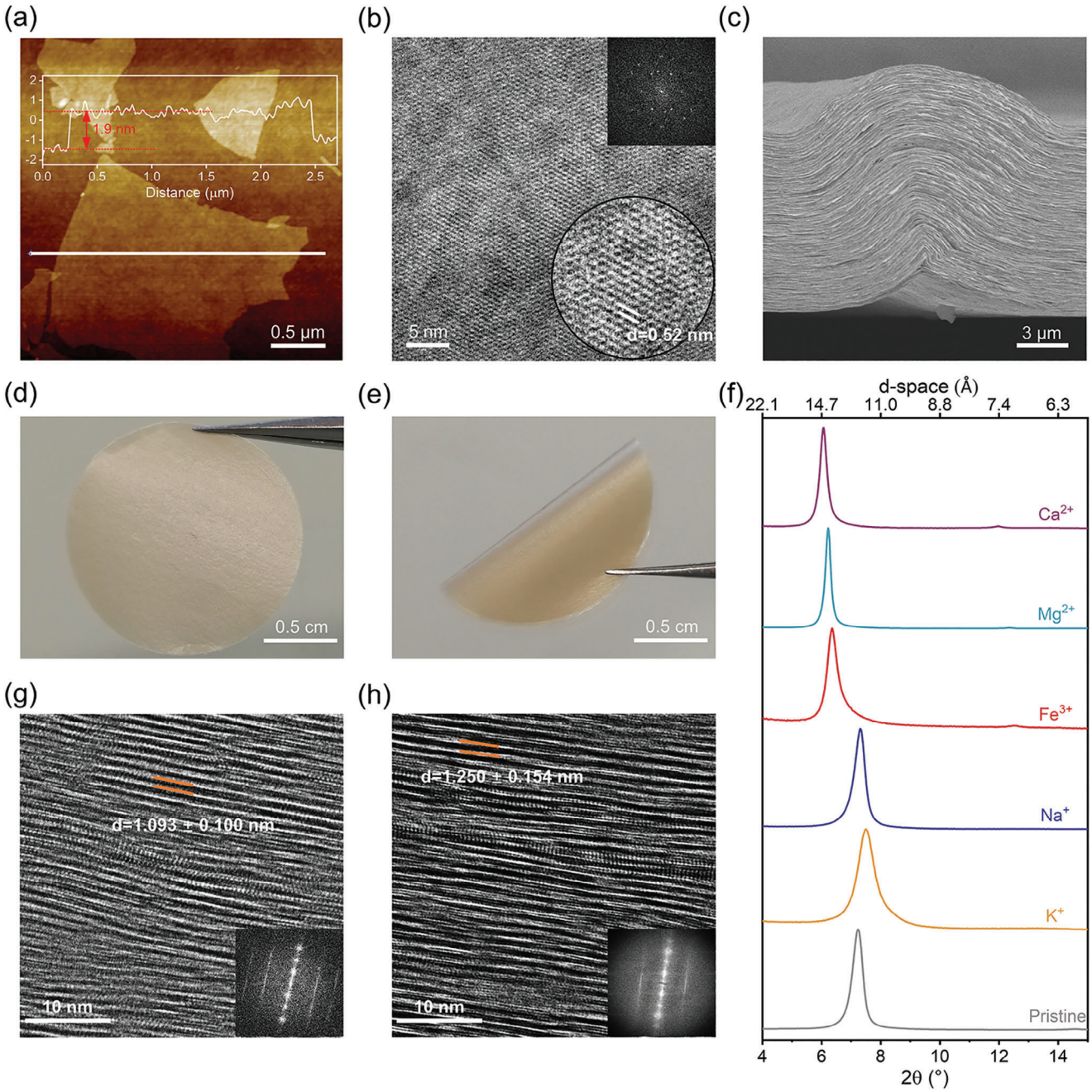

Figure 1. Characterization of vermiculite clay nanosheets and their laminar membranes. a) AFM image of exfoliated clay nanosheets. The inset shows the height profiles taken along the white solid line. b) HRTEM image of a single-layer clay nanosheets. The top inset presents the corresponding Fast Fourier Transform (FFT) pattern, while the bottom inset magnifies the lattice fringes. c) SEM cross-sectional view of the laminated clay membrane. d) An optical photograph of a free-standing K-clay membrane with a thickness of 5 μm. e) Photograph of the K-clay membrane bent with tweezers, demonstrating its resilience and flexibility. f) XRD patterns of pristine and ion-treated clay membranes with a thickness of 1 μm. The membranes were vacuum-dried for 24 h before measurement. g,h) HRTEM images of the cross-sections of pristine (**g**) and Fe-clay (**h**) membranes. The bright regions represent the single-layer clay nanosheets. Inset: the FFT pattern of the image. The d values and the corresponding standard errors are calculated from several images (Figure S4, Supporting Information).

transmembrane. Metal cations reside in the interlayer due to electrostatic attraction (Figure S2 and Table S1 and S2, Supporting Information), acting as cross-linking agents to lock the interlayer space. Excess free cations were thoroughly removed through extensive water washing. The cation-treated membranes exhibit improved mechanical properties, while retaining flexibility (Figure 1d,e and Figure S3, Supporting Information). To characterize the structure of the nanolaminates and evaluate the interlayer spacing, we employed X-ray diffraction (XRD).[17] As shown in Figure 1f, pristine membranes have an interlayer space

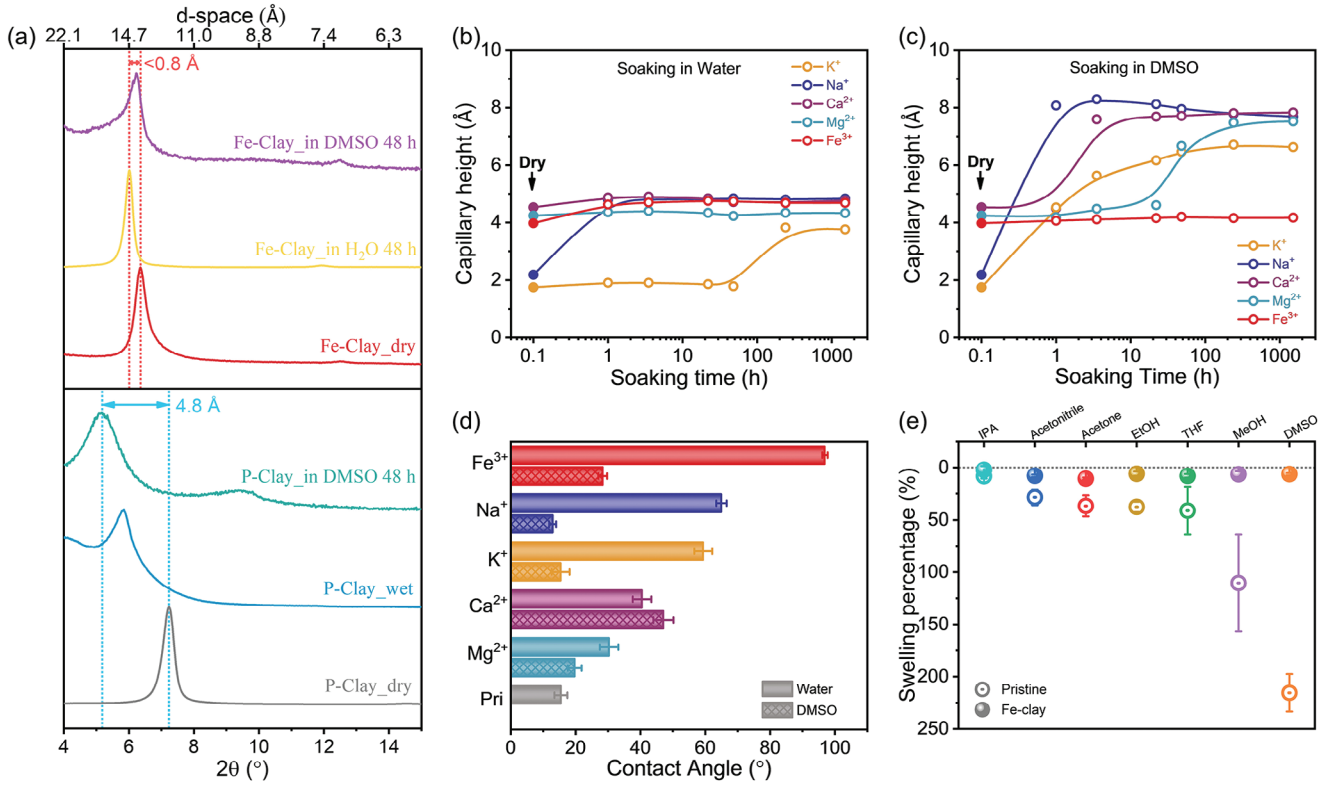

Figure 2. Physicochemical properties of laminar clay membranes with a thickness of 1 µm. a) XRD patterns of pristine and Fe-clay membranes before and after immersion in both aqueous and organic solvents. The as-prepared wet pristine membrane was measured instead of the water-soaked membrane, as the latter rapidly deteriorates upon contact with water. b,c) Evolution of capillary height of different ion-treated clay membranes in water (**b**) and DMSO (**c**) with soaking time. The capillary height was estimated by subtracting 10 Å, corresponding to the thickness of single-layer clay nanosheets, from the interlayer space. The solid dots correspond to the capillary height measured under dry conditions. d) Water and DMSO contact angles of pristine and ion-treated clay membranes. The DMSO droplets immediately spread out on the pristine membrane surface, resulting in a value close to 0°. The data are expressed as mean values, with error bars representing standard deviations (SD) based on three independent measurements. e) Swelling percentage of pristine (hollow circles) and Fe-clay (solid spheres) membrane in various organic solvents under soaking 240 h.

of 1.22 nm according to XRD results. After cation intercalation, the interlayer space expanded due to the volume of the ions themselves (Table S3, Supporting Information), except for K-clay, which showed a slight shrinkage in interlayer space, which could be attributed to the combined effect of intercalation of K ions in the atomic vacancies of the nanosheets and screening of the electrostatic interactions. Figures 1g,h display the HRTEM cross-sectional views of pristine and Fe-clay membranes. The average interlayer space of the pristine membrane is ≈1.09 nm, while Fe-clay membranes display an increased interlayer space with an average of 0.16 nm, consistent with the XRD results (Figure S4, Supporting Information).

The structural stability of 2D clay membranes in both aqueous and organic phases was systematically investigated. We found that the pristine membranes quickly redisperse within 20 min when immersed in water, indicating extreme instability for aqueous applications. In contrast, Fe-clay membranes remain stable when soaked in water for one year, with no visible changes, demonstrating enhanced aqueous stability (Figure S5, Supporting Information). Both pristine and Fe-clay membranes maintain structural integrity in dimethyl sulfoxide (DMSO) without noticeable redispersion (Figure S6, Supporting Information). We employed XRD to quantitatively assess the change of the interlayer space. As shown in **Figure** 2a, the interlayer space of the wet pristine membrane reaches 1.5 nm due to the existence of the hydration layer. Although pristine clay membranes maintain structural integrity in DMSO, the interlayer space exhibits an increased value up to 1.69 nm as DMSO molecules occupy greater volume than water molecules. In contrast, the Fe-clay membranes show a constant interlayer space in both water and DMSO, highlighting the crucial role of trapped ions in improving membrane stability.

To better understand the effect of intercalated ions on membrane structures, we monitored the changes in interlayer space for different intercalated clay membranes after immersion in water (Figure 2b) and DMSO (Figure 2c). These investigations were carried out using ex situ XRD. Clay membranes treated with multivalent cations demonstrate excellent retention of interlayer space, highlighting their resistance against swelling in water. We found that monovalent cations exhibit a weaker role in space fixation as evidenced by the larger increase of the interlayer space. Compared to the rapidly increasing interlayer space of Na-clay membranes, K-clay maintained a stable space for over 50 h, indicating better stability than Na^+ in water. However, all intercalated membranes, with the exception of Fe-clay, experienced a significant increase in interlayer space within a short time, suggesting a low capacity for interlayer space regulation in DMSO.

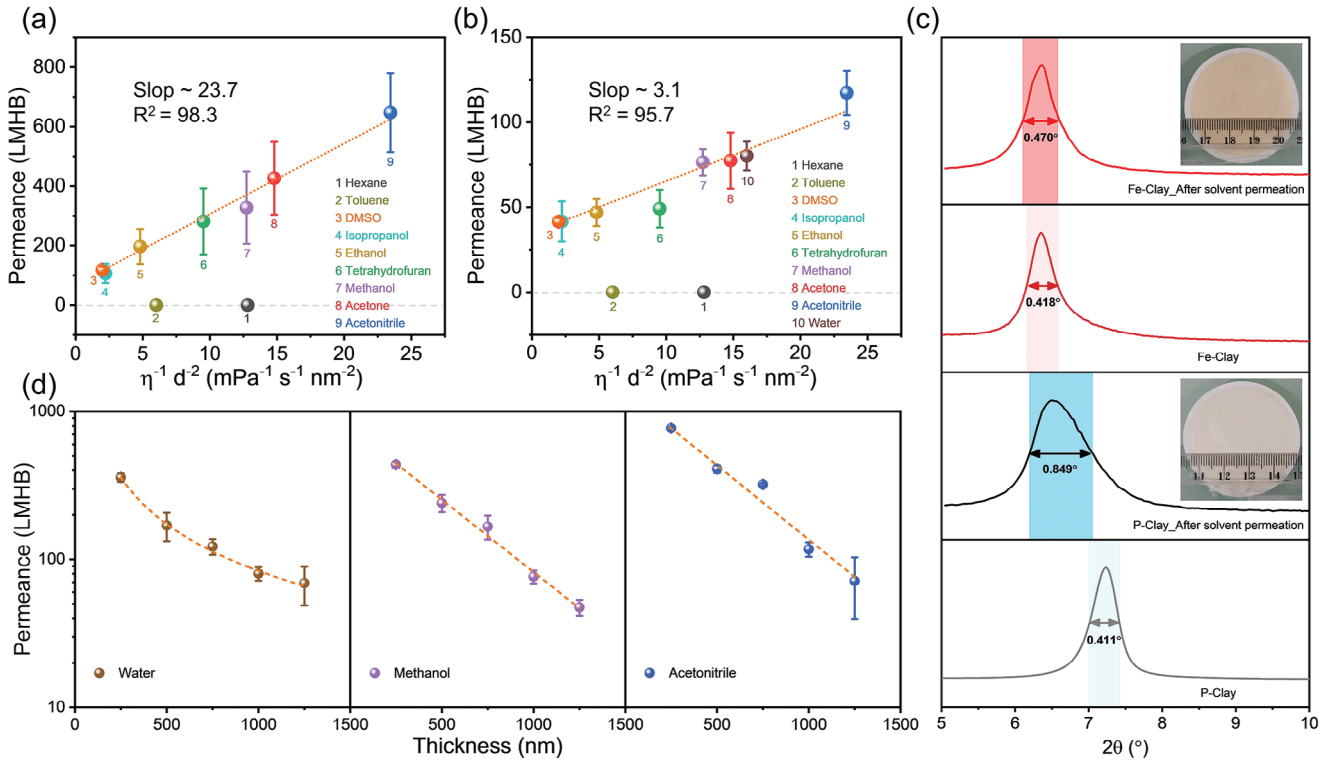

Figure 3. Solvent permeation through the laminar clay membranes. a,b) Permeance of pure polar organic solvents through pristine (**a**) and Fe-clay (**b**) membrane, plotted as a function of the inverse product of their viscosity and kinetic diameter squared. Both pristine and Fe-clay membranes are impermeable to non-polar solvents. The orange dotted lines are the best linear fits. c) Comparison of XRD patterns of pristine and Fe-clay membrane before and after solvent permeation. The FWHM of the XRD peaks is marked and highlighted by the color pillars. Inset: the photographs of the after-measurement membranes. d) Thickness dependence of permeance for water, methanol and acetonitrile through Fe-clay membranes. Water permeance shows an inverse proportionality with membrane thickness, while the permeance of organic solvents exhibits exponential changes. The orange dotted lines represent the best fits. All error bars represent SD derived from at least three independent measurements conducted on distinct samples.

Notably, Fe-clay maintained a robust interlayer space for over two months, implying durable applications in organic phases. Similar behavior was observed with Al^{3+} ions suggesting that the strategy can be extended to other trivalent cations (Figure S7, Supporting Information). The improved stacking order of the Fe-clay membrane was further confirmed by performing rotational orientation XRD measurements (Figure S8, Supporting Information). Additionally, the Fe^{3+} ions residing within the nanochannels can resist ion exchange with other cations present in the feed solution, further strengthening the structural stability of the Fe-clay membrane (Figure S9, Supporting Information). We observed that cation intercalation in clay membranes altered surface wettability (Figure 2d; Figure S10 and S11, Supporting Information), indicating potential for extension to other applications, such as oil/water separation as previously reported by Nair's group.[13b] We further conducted molecular simulations to calculate the interaction forces and found that the dominant interaction is electrostatic attraction between the Fe ions and the negatively charged clay nanosheets.

We further explored the structural changes of pristine and Fe-clay membranes in various organic solvents (Figure S12, Supporting Information). As shown in Figure 2e, pristine membranes underwent dramatic swelling, with the interlayer space expanding by 8% to 215% compared to dry membranes. Among these solvents, IPA induced the mildest increase. In contrast, Fe-clay membranes exhibit limited swelling in all selected solvents. Even for harsh conditions, such as acetone, the maximum swelling was only 10%, emphasizing the remarkably robust nanochannel formation when Fe^{3+} cations reside in the clay interlayer space.

2.2. Solvent Permeation Through 2D Clay Membranes

Because of their remarkable stability, we then investigated the permeation behavior of solvents through nanolaminated clay membranes using a wide range of solvents with varying polarities and molecular sizes (Table S4, Supporting Information). As shown in **Figure 3a**, non-polar solvents like toluene and hexane do not permeate pristine clay membranes. In contrast, polar solvents quickly permeate under pressure and exhibit outstanding flux. Acetonitrile displays the highest permeation rate, exceeding 650 LMHB. We also found that Fe-clay membranes are also impermeable to non-polar molecules (Figure 3b). Our results indicate that for the same thickness, Fe-clay membranes exhibit a ≈75% reduction of the solvent permeance. The reasons for the decreased flux stem from three aspects: limited swelling, improved stacking order and the presence of intercalated ions as discussed later in the manuscript. Due to swelling, the interlayer space in pristine membranes is larger than in

Fe-clay membranes, facilitating solvent diffusion. Besides interlayer space, another important factor is the stacking order of laminated membranes.[17a,c,18] This parameter is often overlooked, but is vital for transport regulation. To evidence this phenomenon, we recorded XRD diagrams of pristine and Fe-clay membranes after solvent permeation. The nanosheets' arrangement in pristine membranes suffered from dramatic adjustment due to weak interactions between adjacent nanosheets, as demonstrated by the enlarged full width at half maximum (FWHM) of XRD peak and theoretical calculations (Figure S13, Supporting Information). A larger FWHM represents a more disordered stacking structure, creating more shortcuts for solvent permeation and leading to higher flux as recently identified by our group.[17c] After undergoing the tortuous transport of solvent molecules, the nanochannels of the pristine membrane expand and could not return to its stacking structure, even in dry conditions (Figure 3c). In contrast, Fe-clay membranes not only maintain their interlayer space but also preserve their stacking order during solvent permeation. The robust nanochannels of Fe-clay membranes would not only benefit solvent transport, but also improve sieving performance. The intercalated ion in the nanochannels would also significantly slow down solvent transport, evidenced by our molecular dynamic simulation (see below in detail).

We found that the permeance of organic polar molecules follows a phenomenological transport model, which is observed in porous inorganic membranes.[19] The permeance (Ps) is correlated to its physical parameters: $P_s = \frac{A}{\eta \times d_{kin}^2}$, where A is a proportionality constant determined by membrane structural parameters, η denotes the solvent viscosity (Pa·s), and d_{kin} is the solvent kinetic diameter (m). Our results show that pristine membranes show a larger proportionality constant than the Fe-clay membranes, as they possess a wider interlayer space, weaker stacking structure, and emptier nanochannel. To explore the transmembrane behavior of water, methanol, and acetonitrile molecules, we prepared Fe-clay membranes with increasing thicknesses up to 1250 nm. As seen in Figure 3d, as membrane thickness increases, the permeance of all tested solvents decreases rapidly due to the extended transmembrane pathway. Notably, the decline in water permeance is slower, presenting a reverse proportional relationship with membrane thickness. In contrast, organic solvents like methanol and acetonitrile exhibit exponential declines, revealing unfavorable transport in thicker membranes. A similar phenomenon was observed by Nair's team on ultrathin GO membranes, attributing it to the transition from gradually disappearing pin-hole transmembrane transport to interlayer transport.[10a] Because all our stacked membranes are quite thick and far from the pin-hole formation regime, we believe that this behavior may be attributed to different natures of the interactions between the solvent and water.

2.3. Molecular Dynamic Simulations of Solvent Transport

To illustrate the behavior of solvent transport in confined nanochannels and the effect of intercalated ions, we conducted classical molecular dynamics simulations of water and methanol molecular transport in a vermiculate nanochannel with and without Fe^{3+}. **Figure** 4a shows a typical simulation cell, where two solvent reservoirs are separated by a nanochannel and external pressure differences are exerted by rigid plates on the leftmost and rightmost sides. The water/methanol flux was first studied under fixed nanochannel height (see Figure 4b). It was observed that water exhibits a higher flux than methanol in nanometer scale channel length, which agrees well with experimental observations when the membrane thickness is extrapolated to the nanometer scale (see Figure 3d). Interestingly, it was observed that water exhibits a more ordered structure than methanol in confined nanochannels (see Figure 4c), which is advantageous for fluidic transport. Simultaneously, water experiences a lower energy barrier (Figure 4d) and greater mobility when entering a confined space from the bulk (Figure 4e), resulting in a higher water flux compared to methanol. Surprisingly, when only one Fe^{3+} is present in the nanochannel, the flux of both water and methanol decrease, demonstrating the significant effect of ion residence on solvent transport. However, the presence of Fe^{3+} in the nanochannel does not alter the distribution structure of solvent molecules, whether they are water or methanol.

We then calculated the velocities of solvent molecules in the flow direction within the radial range centered on the position of Fe^{3+} over the entire simulation time scale and compared it with the situation when there are no Fe atoms in the nanochannel. Figure 4f shows that the presence of Fe^{3+} results in the sum of solvent molecule velocities in the ~8-9 Å range being close to 0, indicating that they do not contribute to fluid flow. This suggests the formation of a sphere of zero-net flux with a diameter of 1.6-1.8 nm centered on Fe^{3+}. The Fe^{3+} fix the solvent molecules within this sphere, hindering their transport. Additionally, the presence of Fe^{3+} makes hydrogen bonds more difficult to break, as evidenced by the increased hydrogen bond lifetime (Figure 4f). Hydrogen bonds act as a net, slowing down the transport of molecules by holding them together. In summary, the synergistic effect of Fe^{3+} anchoring for solvent molecules, and, more rarely, hydrogen bond breaking, leads to a significant drop in solvent flux.

2.4. Nanofiltration for Solvent Purification

To further validate our membranes' defect-free property, we performed separation experiments using organic dyes with negative or positive charges. Eight dyes with different sizes were selected (Table S8, Supporting Information). The rejection of clay membranes was evaluated by measuring the residual dye concentration in the permeated solution using high-performance liquid chromatography (HPLC). The separation performance of Fe-clay membranes was evaluated in both water (**Figure** 5a,b) and methanol (Figure 5d,e). As shown, the membranes demonstrate increased rejection with rising molecular weight, which corresponds to larger molecular size, indicating that size exclusion is the primary sieving mechanism in both water and methanol. To eliminate any potential influence of dye adsorption by the membrane on rejection performance, we assessed the adsorption capacity of the clay membrane for organic dyes and found that the adsorption was negligible (Table S9 and Figure S14, Supporting Information). We also found that negatively charged dyes are better rejected than positively charged dyes by Fe-clay membranes for molecular weights, illustrating the importance of electrostatic interaction in molecular sieving. The 2D clay

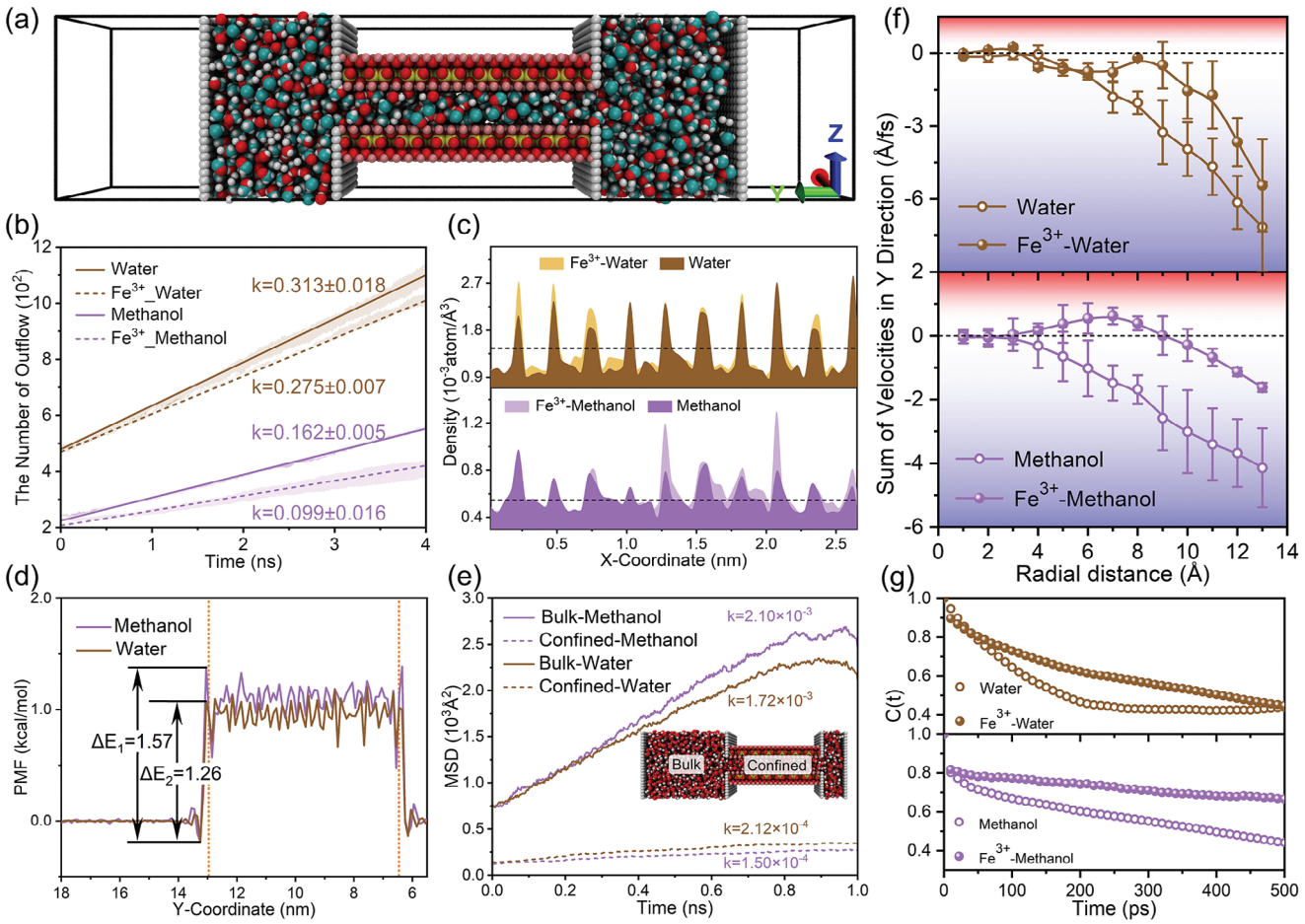

Figure 4. Molecular dynamic simulations of solvent transport. a) Snapshot of a typical atomistic model used in the simulations. b) The number of solvent molecules that passed through the nanochannels with and without Fe^{3+} residence in the MD simulation as a function of simulation time. c) Solvent molecule density distribution in the nanochannel perpendicular to the flow direction. d) The potential of mean force (PMF) profiles for water and methanol passing through the nanochannel. Energy barriers for solvent entry into nanochannels are labeled. e) Mean square displacements of water and methanol molecules in bulk and confined in the nanochannel. f) The sum of the solvent molecule velocities in the flow direction as a function of the radial distance centered on the Fe^{3+} position or nanochannel center (without Fe^{3+} residence in nanochannels) over the entire simulation time scale. Red represents opposing flow, while blue indicates aligned flow, contributing to net flux. g) Hydrogen bond correlation function of solvent molecules confined within nanochannels with and without Fe^{3+} resident. All error bars represent SD derived from three independent simulations.

nanosheets are highly negatively charged due to isomorphism (Figure S15, Supporting Information), resulting from the positive charge loss after $Al^{3+} \rightarrow Si^{4+}$ replacement in the tetrahedral sheet.[20] Although the intercalated Fe^{3+} ions reduce some negative charges, the nanochannel retains a net negative charge, as confirmed by our AFM-scanning Kelvin probe force microscopy (AFM-SKPFM) measurements (Figure S16, Supporting Information). This residual charge helps explain the observed differences in rejection between neutral and charged molecules. Negatively charged molecules are repelled by electrostatic forces, while positively charged molecules strongly interact with the nanosheets, which results in both cases in lower permeation rates. Conversely, the transport of neutral molecules is solely governed by size confinement, resulting in the lowest rejection rates (Figure S17, Supporting Information). We also noticed that the rejection of dye molecules was slightly higher in water than in methanol, which is significantly different from the observation in GO/MXene membranes.[21] For instance, the dye rejection of GO/MXene,[21] such as MO, is much lower in methanol (≈25%) than in water (≈98%), due to the charge difference. The charge of GO and MXene nanosheets originates from the ionization of carboxyl and hydroxyl groups, which results in much higher charges in water than in methanol. However, the surface charge properties of clay nanosheets induced by isomorphism remain unaffected by the solvent, bringing more stable separation performance in different environments. Additionally, we observed reduced solvent permeance in the presence of dye compared to pure solvent filtration, originating from a drop of the driven force due to concentration polarization (CP) and membranes fouling.[22] Furthermore, we investigated the dye separation performance of pristine membranes in methanol for comparison. The strong electric attraction between positive dye molecules and 2D nanosheets, and the weak combination of the nanosheets themselves, coupled with the external stirring, caused the pristine membrane to quickly become jelly-like under stirring and lose its function. Only the separation performance for negatively

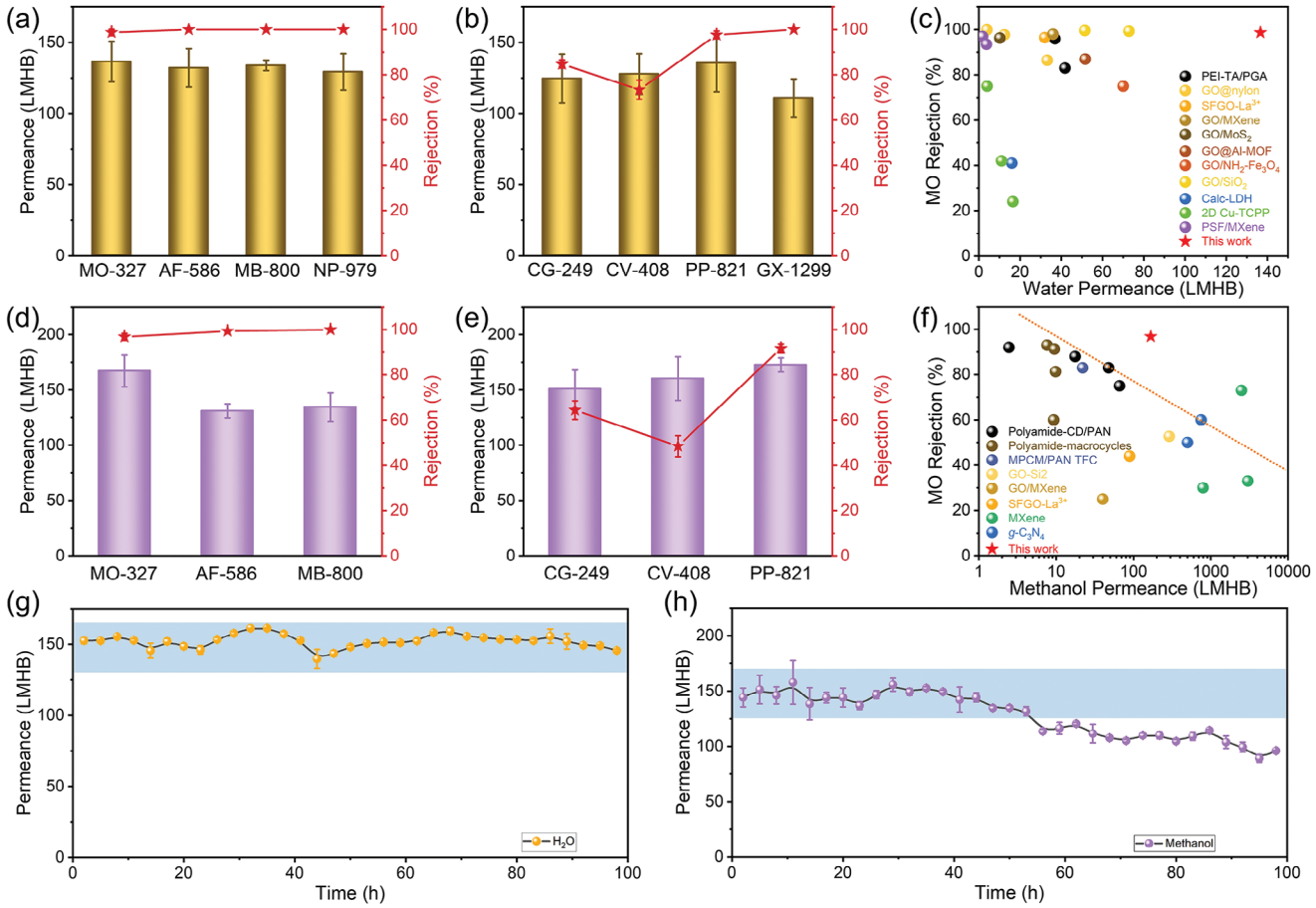

Figure 5. Nanofiltration performance of the 500-nm-thick Fe-clay membranes. a,b) Negatively (**a**) and positively (**b**) charged dyes rejection and water permeance of Fe-clay membranes. The dyes' abbreviations along with their corresponding molecular weights are indicated on the abscissa. c) Comparison of the MO separation performance of Fe-clay membrane in water with that of other 2D materials membranes and their hybrids. A direct comparison can be found in Table S10 (Supporting Information). d,e) Negatively (**d**) and positively (**e**) charged dyes rejection and methanol permeance of Fe-clay membrane. f) Comparison of the MO separation performance in methanol of Fe-clay membrane against state-of-the-art membranes. The orange dotted line in the figure serves as a visual aid, indicating the upper-performance boundary of state-of- the-art membranes. Detailed data are included in Table S11 (Supporting Information). g,h) Water (**g**) and methanol (**h**) permeance measured under a tangential cross-flow filtration cell for constant operation over 100 h. All error bars denote SD.

charged dyes could be evaluated (Figure S18, Supporting Information). The pristine membrane shows poor rejection of 25% for MO, compared to > 95% in Fe-clay membranes, highlighting the importance of interlayer space robustness for highly efficient sieving performance. In summary, by combining size confinement and electrostatic interaction, Fe-clay membranes exhibit outstanding molecular sieving ability with unparalleled solvent permeance. Their performance outperforms the current state-of-the-art membranes (Figure 5c–f), making these Fe-clay membranes as promising candidates for organic solvent purification.

To further gauge the applicability of Fe-clay membranes for realistic separation application, we incorporated them into a tangential cross-flow filtration cell for constant permeation operation. The solvent flux of the Fe-clay membranes was continuously monitored over the operating time for 100 h. As illustrated in Figure 5g, the Fe-clay membrane demonstrates stable water permeation, confirming its suitability for long-term membrane applications. Although the methanol permeance exhibits a slight decrease during filtration (Figure 5h), the Fe-clay membranes still possess ultrafast methanol transport ability with a flow rate of over 100 LMHB after four days. This exceptional stability of Fe-clay surpasses the state-of-the-art 2D laminar membranes, which typically exhibit a short operation time of less than 24 h under pressure.[11b,14a,21]

3. Conclusion

In conclusion, we have successfully developed Fe-clay nanolaminated membranes with exceptional structural stability and outstanding separation performance for both aqueous and organic solvent purification. By combining structural analyses, separation testing and molecular dynamic simulations, we identified the crucial role of Fe^{3+} in maintaining interlayer space stability and enhancing molecular sieving properties of the clay nanolaminates. We demonstrate that Fe-intercalated vermiculite nanolaminated membranes exhibit excellent dye separation performance, surpassing the capabilities of current state-of-the-art membranes. This combined with their long-term operational

stability makes the Fe-clay membranes remarkable candidates for practical applications in organic solvent filtration.

4. Experimental Section

Synthesize of Single-Layer Vermiculate Nanosheets: The monolayer vermiculite nanosheets were prepared through a series of exfoliation and ion-exchange processes. First, 1g of non-thermally expanded bulk vermiculite clay crystals were added to 200 mL of saturated NaCl solution, refluxing for 24 h under vigorous stirring to obtain Na-exchanged clay. The Na-exchanged clay was then collected by filtration and washed extensively with deionized water (DI) to remove residual NaCl. Subsequently, the collected clay was dispersed in a 2 M LiCl solution for Na^+ to Li^+ ion exchange, refluxing, and stirring for 24 h. The solution was filtered, and the collected Li-intercalated clay was washed thoroughly with DI water to eliminate any remaining Li ions. The filtered product was then dispersed in water and stirred at 1000 rpm for 24 h to enable hydraulic shear peeling. After that, this solution was sonicated for 30 min to facilitate the exfoliation process. Finally, the single-layer clay nanosheets were collected from the supernatant after mild centrifugation at 3000 rpm for 30 min.

Preparation of Pristine and Cation-Treated Clay Membranes: The pristine clay membranes were fabricated by pressure-assisted filtration of diluted single-layer nanosheet solutions. Specifically, a certain volume of clay solution was filtered onto a 220 nm pore-sized Nylon support using 1 bar of pressure. To prepare cation-treated clay membranes, 10 mL of different chloride salts (KCl, NaCl, $CaCl_2$, $MgCl_2$, and $FeCl_3$) at a concentration of 0.25 M were added to the pristine membranes. After waiting for 3 h to allow for ion diffusion and cross-linking, a 1 bar pressure was applied to force the salt solution through the membrane, promoting ion traversal and achieving complete cation cross-linked nanochannels. Next, 50 mL of DI water was added and the membranes were subjected to a pressure of 1 bar to wash away the excess of ions. This process resulted in the formation of cation-treated clay membranes.

Solvent Permeation Through Nanolaminated Clay Membranes: Nine types of organic solvents, including hexane, toluene, isopropanol (IPA), dimethyl sulfoxide (DMSO), ethanol, tetrahydrofuran (THF), acetone, methanol, and acetonitrile, were used to examine the permeation behavior through 1-µm-thick pristine and Fe-clay membranes using a reverse osmosis filtration cell. In this setup, the organic solvent was added, and a pressure of 1 bar was applied as a driving force for the solvent to cross the membranes. The weight of the passed solvent was automatically recorded by a balance and used to evaluate the flux. The solvent permeance (liter m^{-2} $hour^{-1}$ bar^{-1}, LMHB) was calculated using the following equation:

$$P_s = \frac{W}{\Delta p\, A\, t\, \rho} \tag{1}$$

where W represents the collected solvent mass (kg), Δp denotes the hydraulic pressure (bar), A is the effective membrane area (m^2), t stands for the permeation time (h), and ρ refers to the solvent density (kg L^{-1}). In our dead-end configuration, membranes with an effective area of 13.8 cm^2 were used for measurements. Additionally, the water permeance was evaluated only for Fe-clay membranes, as obtaining this measurement for pristine membranes is challenging due to their rapid redispersion in water.

Solvent Purifications Performance Evaluation: The rejection capacity of clay membranes was evaluated using a high-pressure stirred cell under a dead-end configuration. Eight different organic dyes including chrysoidine G (CG), methyl orange (MO), crystal violet (CV), acid fuchsin sodium salt (AF), methyl blue (MB), 5,10,15,20-(tetra-N-methyl-4-pyridyl) porphyrin tetrachloride (PP), nickel(II) phthalocyanine-tetrasulfonic acid tetrasodium salt (NP) and alcian blue 8GX (GX) were each dissolved in water or methanol to form feed solutions with a concentration of 25 ppm, which were then filtered through a 500-nm-thick clay membrane at 1-bar pressure. Due to the poor solubility of NP and GX in methanol, only six of the dyes were measured using methanol feed solutions. The rejection rates of clay membranes for the dyes, R (%), were calculated using the following equation:

$$R\ (\%) = \left(1 - \frac{C_p}{C_f}\right) \times 100 \tag{2}$$

where C_p and C_f represent the concentration of the organic dyes in the permeate and feed solution, respectively. The concentrations of dyes in the collected solutions were quantitatively analyzed by HPLC coupled with mass spectrometry.

Membrane Stability Evaluation in a Tangential Cross-Flow Filtration Cell: We utilized a tangential cross-flow filtration cell to evaluate the long-term stability of the Fe-clay membranes under solvent permeation. Pure water or methanol solution was circulated in the system, with the Fe-clay membranes positioned between the feed and permeate sides of the cell. A peristaltic pump ensured a consistent flow rate of 8.54 ml min^{-1} while maintaining a pressure of 1 bar. A tube with an inner diameter of 0.5 cm was used for cycling the feed solution, showing a cross-flow velocity of 43.5 cm min^{-1}. The permeated solvent was collected and weighed using balances, allowing for the calculation of flux throughout the experiment.

Molecular Dynamics Simulations: All the molecular dynamics simulations were performed in the large-scale atomic/molecular massively parallel simulator (LAMMPS) software. The Optimized Potentials for Liquid Simulations All-Atom (OPLS-AA) force field described the fluid molecules, and the mineral was described by the force field of Clay-FF, which the charges were obtained by Dmol3 (see Supplementary Information). The cutoff distance for all the short-range van der Waals (vdW) interactions was set as 12 Å. The long-range electrostatic interactions were computed by using the particle-particle particle-mesh (PPPM) algorithm. The simulation was conducted in a canonical ensemble (NVT) at 298 K controlled by the Nose-Hoover thermostat method. The time step was set as 1 fs, and the data were collected every 1 ps. All-atom molecular dynamics simulation was performed for a total of 6 ns. The first 1 ns was used for equilibrium molecular dynamics (EMD) simulation to obtain a reasonably stable configuration. During the equilibrium process, a pressure of 1 bar was applied to both sides to ensure sufficient penetration of the liquid into the interlayer of clay. In the subsequent 5 ns, the pressure applied to the input was increased to 600 MPa to provide the driving force for transport. Higher pressure was employed to expedite the simulation time. Simultaneously, a spring force constraint was imposed on the Fe atom to ensure that it did not experience excessive deviation. Each simulation was run three times with distinct initial velocity distributions.

Supporting Information

Supporting Information is available from the Wiley Online Library or from the author.

Acknowledgements

This research study was supported by the French National Agency (ANR, program 2D-MEMBA – ANR-21-CE09-0034-01). D.V., W.W., K.Q., and H.W. acknowledge funding from the European Research Council (ERC) under the European Union's Horizon 2020 research and innovation programme (grant agreement no. 804320). W.W., J.L. and J-F.L. acknowledge the scholarship from the China Scholarship Council (CSC). C.S. acknowledges funding from the French National Agency (ANR, JCJC program, MONOME – ANR-20-CE08-0009). L.L. acknowledges funding the from the Spanish Ministerio de Economía y Competitividad, the Ministerio de Ciencia e Innovación MCIN/AEI/10.13039/501100011033/FEDER UE, and the European Union "NextGenerationEU"/PRTR (PID2022-140370NB-I00, RYC2021-033764-I, CPP2021-008986). The (S)TEM measurements were performed at the National Facility ELECMI ICTS ("División de Microscopía Electrónica", Universidad de Cadiz, DME-UCA).

Conflict of Interest

The authors declare no conflict of interest.

Data Availability Statement

The data that support the findings of this study are available in the supplementary material of this article.

Keywords

2D materials, cations intercalations, nanolaminated membranes, non-covalent functionalization, organic solvent nanofiltration

Received: June 18, 2024
Revised: November 19, 2024
Published online: December 6, 2024

[1] a) E. Obotey Ezugbe, S. Rathilal, *Membranes* **2020**, *10*, 89; b) Y. J. Lim, K. Goh, M. Kurihara, R. Wang, *J. Membr. Sci.* **2021**, *629*, 119292.
[2] a) Z. Yang, Y. Zhou, Z. Feng, X. Rui, T. Zhang, Z. Zhang, *Polymers* **2019**, *11*, 1252; b) M. Bassyouni, M. Abdel-Aziz, M. S. Zoromba, S. Abdel-Hamid, E. Drioli, *J. Ind. Eng. Chem.* **2019**, *73*, 19.
[3] a) P. Marchetti, M. F. Jimenez Solomon, G. Szekely, A. G. Livingston, *Chem. Rev* **2014**, *114*, 10735; b) A. M. Tandel, W. Guo, K. Bye, L. Huang, M. Galizia, H. Lin, *Mater. Adv.* **2021**, *2*, 4574; c) S. Ali, I. A. Shah, I. Ihsanullah, X. Feng, *Chemosphere* **2022**, *308*, 136329; d) G. M. Shi, Y. Feng, B. Li, H. M. Tham, J. Y. Lai, T. S. Chung, *Prog. Polym. Sci.* **2021**, *123*, 101470; e) Z. Wang, X. Luo, J. Zhang, F. Zhang, W. Fang, J. Jin, *Advanced Membranes* **2023**, *3*, 100063.
[4] a) M. Buonomenna, J. Bae, *Sep. Purif. Rev.* **2015**, *44*, 157; b) K. Werth, P. Kaupenjohann, M. Skiborowski, *Sep. Purif. Technol.* **2017**, *182*, 185; c) R. P. Lively, D. S. Sholl, *Nat. Mater.* **2017**, *16*, 276; d) C. Zamora-Ledezma, D. Negrete-Bolagay, F. Figueroa, E. Zamora-Ledezma, M. Ni, F. Alexis, V. H. Guerrero, *Environ. Technol. Inno.* **2021**, *22*, 101504; e) D. Negrete-Bolagay, C. Zamora-Ledezma, C. Chuya-Sumba, F. B. De Sousa, D. Whitehead, F. Alexis, V. H. Guerrero, *J. Environ. Manage.* **2021**, *300*, 113737.
[5] F. R. Fan, R. Wang, H. Zhang, W. Wu, *Chem. Soc. Rev.* **2021**, *50*, 10983.
[6] V. K. Sangwan, M. C. Hersam, *Annu. Rev. Phys. Chem.* **2018**, *69*, 299.
[7] X. Chen, H. Yu, Y. Gao, L. Wang, G. Wang, *EnergyChem* **2022**, *4*, 100071.
[8] a) G. Liu, W. Jin, N. Xu, *Angew. Chem., Int. Ed.* **2016**, *55*, 13384; b) P. Liu, J. Hou, Y. Zhang, L. Li, X. Lu, Z. Tang, *Inorg. Chem. Front.* **2020**, *7*, 2560.
[9] a) L. Cheng, G. Liu, J. Zhao, W. Jin, *Acc. Mater. Res.* **2021**, *2*, 114; b) S. Wang, L. Yang, G. He, B. Shi, Y. Li, H. Wu, R. Zhang, S. Nunes, Z. Jiang, *Chem. Soc. Rev.* **2020**, *49*, 1071.
[10] a) Q. Yang, Y. Su, C. Chi, C. Cherian, K. Huang, V. Kravets, F. Wang, J. Zhang, A. Pratt, A. Grigorenko, *Nat. Mater.* **2017**, *16*, 1198; b) R. Nair, H. Wu, P. N. Jayaram, I. V. Grigorieva, A. Geim, *Science* **2012**, *335*, 442; c) X. Sui, Z. Yuan, Y. Yu, K. Goh, Y. Chen, *Small* **2020**, *16*, 2003400.
[11] a) B. Y. Guo, S. D. Jiang, M. J. Tang, K. Li, S. Sun, P. Y. Chen, S. Zhang, *J. Phys. Chem. Lett.* **2019**, *10*, 4609; b) J. Ran, P. Zhang, C. Chu, P. Cui, X. Ai, T. Pan, Y. Wu, T. Xu, *J. Membr. Sci* **2020**, *602*, 117963; c) J. Wang, P. Chen, B. Shi, W. Guo, M. Jaroniec, S. Z. Qiao, *Angew. Chem., Int. Ed.* **2018**, *57*, 6814; d) X. Wu, X. Cui, W. Wu, J. Wang, Y. Li, Z. Jiang, *Angew. Chem., Int. Ed.* **2019**, *58*, 18524.
[12] a) X. Cai, Y. Luo, B. Liu, H. M. Cheng, *Chem. Soc. Rev.* **2018**, *47*, 6224; b) W. Zheng, L. Y. S. Lee, *Matter* **2022**, *5*, 515.
[13] a) J. J. Shao, K. Raidongia, A. R. Koltonow, J. Huang, *Nat. Commun* **2015**, *6*, 7602; b) K. Huang, P. Rowe, C. Chi, V. Sreepal, T. Bohn, K. G. Zhou, Y. Su, E. Prestat, P. B. Pillai, C. Cherian, *Nat. Commun* **2020**, *11*, 1097; c) M. Li, Y. Zhao, Z. Ai, H. Bai, T. Zhang, S. Song, *Chem. Phys.* **2021**, *550*, 111313.
[14] a) M. Tian, L. Wang, J. Wang, S. Zheng, F. Wang, N. Shao, L. Wang, *ACS Sustainable Chem. Eng.* **2022**, *10*, 1137; b) J. Wang, Z. Cui, S. Li, Z. Song, M. He, D. Huang, Y. Feng, Y. Liu, K. Zhou, X. Wang, *Nat. Commun.* **2024**, *15*, 608; c) X. Wei, Y. Liu, Z. Zhang, F. Zhao, Z. Li, C. Fan, Y. Yang, Z. Jiang, *J. Membr. Sci.* **2024**, *695*, 122461; d) Y. Feng, S. Li, H. Lu, L. Lei, Q. Rong, Z. Su, D. Zhang, X. Wang, L. Wang, J. Wang, *ACS Nano* **2024**, *18*, 32797.
[15] a) C. N. Yeh, K. Raidongia, J. Shao, Q. H. Yang, J. Huang, *Nat. Chem* **2015**, *7*, 166; b) L. Chen, G. Shi, J. Shen, B. Peng, B. Zhang, Y. Wang, F. Bian, J. Wang, D. Li, Z. Qian, *Nature* **2017**, *550*, 380; c) L. Ding, L. Li, Y. Liu, Y. Wu, Z. Lu, J. Deng, Y. Wei, J. Caro, H. Wang, *Nat. Sustain.* **2020**, *3*, 296.
[16] A. M. Mathieson, G. Walker, *Am. Min.* **1954**, *39*, 231.
[17] a) L. Ries, E. Petit, T. Michel, C. C. Diogo, C. Gervais, C. Salameh, M. Bechelany, S. Balme, P. Miele, N. Onofrio, *Nat. Mater.* **2019**, *18*, 1112; b) J. Abraham, K. S. Vasu, C. D. Williams, K. Gopinadhan, Y. Su, C. T. Cherian, J. Dix, E. Prestat, S. J. Haigh, I. V. Grigorieva, *Nat. Nanotechnol.* **2017**, *12*, 546; c) W. Wang, N. Onofrio, E. Petit, B. A. Karamoko, H. Wu, J. Liu, J. Li, K. Qi, Y. Zhang, C. Gervais, *Nat. Water* **2023**, *1*, 187.
[18] X. Lu, U. R. Gabinet, C. L. Ritt, X. Feng, A. Deshmukh, K. Kawabata, M. Kaneda, S. M. Hashmi, C. O. Osuji, M. Elimelech, *Environ. Sci. Technol.* **2020**, *54*, 9640.
[19] A. Buekenhoudt, F. Bisignano, G. De Luca, P. Vandezande, M. Wouters, K. Verhulst, *J. Membr. Sci* **2013**, *439*, 36.
[20] L. Xie, J. Tang, R. Qin, Q. Zhang, J. Liu, Y. Jin, H. Wang, *Adv. Funct. Mater.* **2023**, *33*, 2208959.
[21] S. Wei, Y. Xie, Y. Xing, L. Wang, H. Ye, X. Xiong, S. Wang, K. Han, *J. Membr. Sci.* **2019**, *582*, 414.
[22] L. Nie, K. Goh, Y. Wang, J. Lee, Y. Huang, H. E. Karahan, K. Zhou, M. D. Guiver, T. H. Bae, *Sci. Adv.* **2020**, *6*, eaaz9184.